

Enhancement effects of interlayer orbital hybridization in Janus MoSSe and tellurene heterostructures for photovoltaic applications

Bin Zhou (周斌),¹ Anyang Cui (崔安阳) ¹ Lichen Gao (高立宸),¹ Kai Jiang (姜凯),¹ Liyan Shang (商丽燕),¹ Jinzhong Zhang (张金中),¹ Yawei Li (李亚巍) ¹ Shi-Jing Gong (龚士静),^{2,*} Zhigao Hu (胡志高) ^{1,3,4,†} and Junhao Chu (褚君浩)^{1,3,4}

¹Technical Center for Multifunctional Magneto-Optical Spectroscopy, Engineering Research Center of Nanophotonics & Advanced Instrument (Ministry of Education), Department of Materials, School of Physics and Electronic Science, East China Normal University, Shanghai 200241, China

²Department of Physics, School of Physics and Electronic Science, East China Normal University, Shanghai 200241, China

³Collaborative Innovation Center of Extreme Optics, Shanxi University, Taiyuan, Shanxi 030006, China

⁴Shanghai Institute of Intelligent Electronics & Systems, Fudan University, Shanghai 200433, China



(Received 20 July 2021; revised 10 November 2021; accepted 15 November 2021; published 9 December 2021)

Interlayer orbital hybridization plays a crucial role in the design of optoelectronic, photovoltaic, and photocatalysis devices based on stacked van der Waals (vdW) materials. In this work, using first-principles calculations, we report an enhancement phenomenon of interlayer orbital hybridization at MoSSe/tellurene (Te) vdW interface. The charge density of two components in MoSSe/Te are overlapped at conduction band minimum, which features highly efficient excitonic solar cells with power conversion efficiency (PCE) up to 22.6%. Moreover, the MoSSe/Te heterostructure exhibits a remarkable absorbance coefficient up to $\sim 7 \times 10^5 \text{ cm}^{-1}$ from ultraviolet (UV) to visible light region. Combined with the nonequilibrium Green's function (NEGF) method, the calculated maximum photoinduced current density under visible light radiation from the heterobilayer is up to 3.2 mA cm^{-2} , which remarkably exceeds those of the thin-film silicon and bilayer MoSSe devices. Finally, the superior photocatalytic activities are revealed and discussed. Our present findings confirm that the heterostacking of Janus MoSSe and Te could be strikingly helpful for optoelectronic, photovoltaic, and photocatalytic applications.

DOI: [10.1103/PhysRevMaterials.5.125404](https://doi.org/10.1103/PhysRevMaterials.5.125404)

I. INTRODUCTION

Two-dimensional (2D) materials with layered structure are found to have a remarkable excitonic effect due to their weak dielectric screening effects, which provides an unprecedented opportunity in exploring novel applications, such as exciton solar cells and photodetectors [1]. Meanwhile, the effects of van der Waals (vdW) interlayer orbital hybridization in 2D materials to generate quantum phenomena are unraveled in recent years, such as Mott insulating [2], superconductivity [3], and topological polaritons [4]. Thus, the interlayer hybridization can significantly promote the fundamental understanding and drive the device applications based on 2D vdW heterostructures. Recently, a new monolayer, the Janus MoSSe, has been experimentally realized by selenization or sulfurization [5,6]. In contrast to conventional transition metal dichalcogenide (TMD), the chalcogens on one side of Janus MoSSe are different from those on the other side. It has broken mirror symmetry to the basal plane and an intrinsic out-of-plane dipole moment due to the electronegativity difference between the chalcogens [7]. The broken symmetry of Janus TMDs leads to

extraordinary optical and electronic properties, which are absent in conventional TMDs. For example, it has been demonstrated experimentally that lacking of mirror symmetry in monolayer MoSSe can induce out-of-plane piezoelectricity, incident angle-dependent second harmonic generation, and surface-enhanced Raman scattering of biomolecules [5,8]. Furthermore, the intrinsic polarization field of Janus MoSSe contributes to effective carriers separation [9], extra-long exciton lifetime [10], and remarkable photocatalytic water splitting [11–13], which can help to realize multifunctional device applications.

As a new member of the elementary 2D materials family, the existence of β -tellurene (Te) with its monolayer or few-layer form, has been predicted or confirmed by theoretical and experimental works [14–18]. The bulk β -Te has a trigonal crystal lattice with one-dimensional helical chains, which are covalently bonded with threefold screw axis symmetry and form a trigonal lattice through van der Waals interaction. Due to its superior optoelectronics properties [19–21], such as a suitable direct band gap (1.47 eV) and higher mobility ($2.87 \times 10^3 \text{ cm}^2 \text{ V}^{-1} \text{ s}^{-1}$), β -tellurene is considered as a successor of silicon and has been applied in various optoelectronic fields.

In excitonic solar cells, power conversion efficiency depends critically on the interface band alignment between donor and acceptor materials. For example, Yang *et al.*

*sjgong@ee.ecnu.edu.cn

†zghu@ee.ecnu.edu.cn

constructed excitonic solar cells based on 2D heterojunctions between tellurene and transition metal dichalcogenide, which display remarkable sunlight absorption and the maximum PCE for Te/MoTe₂ and Te/WTe₂ can reach even as high as 20.1% and 22.5%, respectively [22]. In this work, the Janus MoSSe and Te monolayers are selected to construct MoSSe/Te and MoSeS/Te vdW heterostructures. An enhancement phenomenon of interlayer orbital hybridization in vdW heterostructure interface that involve polar Janus TMDs is expected. It is found that both MoSSe/Te and MoSeS/Te exhibit type-II band alignment with band gaps of 1.50 and 1.05 eV, respectively. The calculated maximum power conversion efficiency (PCE) of our designed MoSSe/Te excitonic solar cells can reach as high as 22.6%, which is superior to most of other 2D heterojunction solar cells. Furthermore, we propose that both MoSSe/Te and MoSeS/Te heterobilayers can be used as high efficient photocatalysts for splitting water into hydrogen and oxygen. These theoretical results can open promising potential energy applications from Janus MoSSe and tellurene vdW heterostructures.

II. COMPUTATIONAL DETAILS

The first-principles calculations were performed based on density functional theory (DFT), using a projector augmented-wave method as implemented in the Vienna *ab initio* simulation package (VASP) code [23–25]. The exchange correlation functional was used within generalized gradient approximation with the Perdew-Burke-Ernzerhof (GGA-PBE) [26,27]. A plane-wave basis set with a cutoff of 450 eV was used and a k mesh of $4 \times 9 \times 1$ was adopted to sample the first Brillouin zone of the monolayers and heterostructures. The conjugate-gradient scheme is applied for the geometric optimization until the force on each atom is less than $0.01 \text{ eV } \text{Å}^{-1}$, and the total energy change is less than 10^{-6} eV to acquire good convergence. A sufficient vacuum space ($\geq 25 \text{ Å}$) is used along the z direction to avoid periodicity interaction between adjacent images. A semiempirical dispersion potential to the Kohn-Sham DFT energy is considered through a pairwise force field following the Grimme's DFT-D2 method [28]. Because of the intrinsic dipole in the MoSSe monolayer, a dipole correction in its normal direction is included [29]. A Heyd-Scuseria-Ernzerhof (HSE06) hybrid functional is included to give better electronic structure pictures [30]. In fact, excitonic interactions methods have been used in many previous researches about the electronic and photoelectronic transport properties of pristine 2D materials. And it is found that although excitonic interactions methods can give more accurate results, the band structures of HSE calculation are quantitatively in agreement with those from the excitonic interactions methods [9,10,14]. Thus, in this work, considering the huge cost of the computing resources, we only performed the electronic properties of MoSSe/Te vdWH based on the HSE functional in this work, we believe the conclusions should still be valid.

In order to design and investigate the Janus MoSSe and β -Te combined vdW heterostructures, a lattice matched supercell with less strains is an essential requirement. Therefore, the MoSSe/Te and MoSeS/Te heterostructures are constructed using $1 \times 4 \times 1$ MoSSe rectangular supercell and $1 \times 3 \times 1$

Te supercell, as shown in Figs. 2(a) and 2(b). The lattice mismatch along both x and y directions is less than 2%, which is located in a reasonable range and leads to reliable computational results. To quantitatively evaluate the relative stability of the heterostructures, the binding energy (E_b) are calculated by $E_b = E_{\text{Hetero}} - (E_{\text{MoSSe}} + E_{\text{Te}})$, where E_{Hetero} , E_{MoSSe} , and E_{Te} represent the total energies of the heterobilayers, MoSSe, and β -Te monolayers, respectively.

As the absorption range of the spectrum is very important in the application of optoelectronic devices, we calculate the optical absorption coefficient by using the follow formula:

$$\alpha(\omega) = \sqrt{2\omega}[\sqrt{\epsilon_1(\omega)^2 + \epsilon_2(\omega)^2} - \epsilon_1(\omega)]^{1/2}, \quad (1)$$

where ϵ_1 and ϵ_2 are the real part and imaginary part of the complex dielectric function, and the ϵ_1 could be obtained from ϵ_2 by the Kramer-Kronig relationship. The ϵ_2 is defined as

$$\epsilon_2(\omega) = \frac{4\pi^2 e^2}{\Omega} \lim_{q \rightarrow 0} \frac{1}{q^2} \sum_{c,v,\vec{k}} 2w_k \delta(\epsilon_{ck} - \epsilon_{vk} - \omega) \times \langle \mu_{ck+e_\alpha} | \mu_{vk} \rangle \langle \mu_{ck+e_\beta} | \mu_{vk}^* \rangle, \quad (2)$$

here α and β represent the x and y directions, and Ω is the volume of the unit cell. The indices c and v refer to the conduction and valence band states, respectively. μ_{ck} corresponds to an eigenstate with wave vector k .

Furthermore, the photocurrent density is calculated based on the nonequilibrium Green's function-DFT method, as implemented in quantum ATK software [31]. The detailed

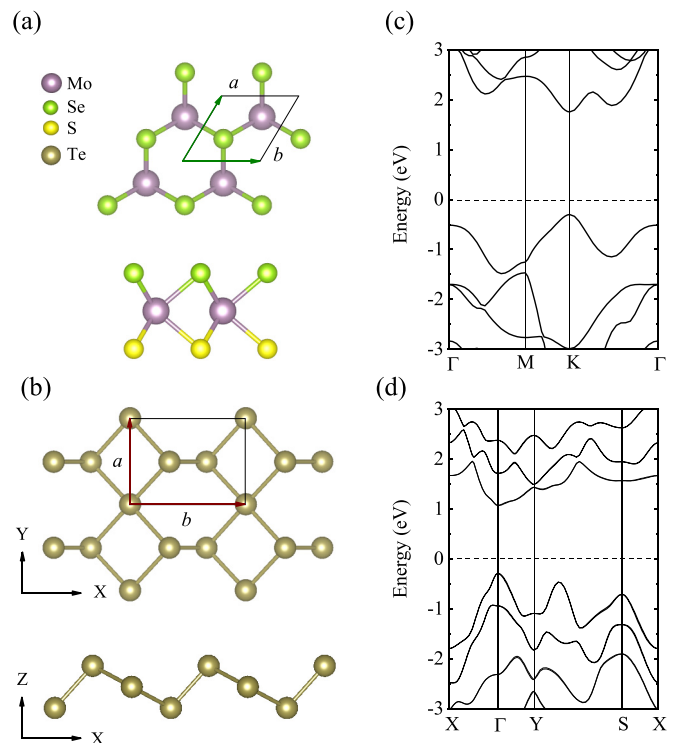


FIG. 1. (a) and (b) Top and side views of the lattice structure of Janus MoSSe and β -Te monolayers. (c) and (d) The calculated band structures of Janus MoSSe and β -Te monolayers. The exchange associated functionals HSE06 are used to compute the electronic band structures.

TABLE I. Calculated carrier effective masses m_x^* for electron (e) and hole (h) along x and y directions for the corresponding individual layers at room temperature.

	Carrier type	m_x^*/m_0	m_y^*/m_0
Tellurene	electron	0.72	0.17
	hole	0.32	0.11
MoSSe	electron	0.74	0.77
	hole	0.136	0.36

descriptions of this method can be found in previous studies [32–35], which is given by

$$I_\alpha = \frac{e}{h} \int_{-\infty}^{\infty} \sum_{\beta=L,R} [1 - f_\alpha(E)] f_\beta(E - \hbar\omega) T_{\alpha,\beta}^-(E) - f_\alpha(E) [1 - f_\beta(E + \hbar\omega)] T_{\alpha,\beta}^+(E) dE, \quad (3)$$

$$T_{\alpha,\beta}^-(E) = N \text{Tr} \{ M^\dagger \tilde{A}_\alpha(E) M A_\beta(E - \hbar\omega) \}, \quad (4)$$

$$T_{\alpha,\beta}^+(E) = N \text{Tr} \{ M \tilde{A}_\alpha(E) M^\dagger A_\beta(E + \hbar\omega) \}, \quad (5)$$

where f is Fermi-Dirac distribution function of electrode α ($\alpha \in L, R$), $A_\alpha = G \Gamma_\alpha G^\dagger$ is the spectral function of electrode α , and G and G^\dagger are retarded and advanced Green's functions, respectively. The electron-photon hybridization matrix is given by

$$M_{\text{ml}} = \frac{e}{m_0} \left(\frac{\hbar \sqrt{\mu_r \epsilon_r}}{2N\omega \tilde{\epsilon} c} F \right)^{1/2} \mathbf{e} \cdot \mathbf{P}_{\text{ml}}. \quad (6)$$

Here the total photocurrent is current discrepancy between two electrodes. Γ_α is spectral broadening, and the momentum operator \mathbf{P}_{ml} is calculated by nonequilibrium Green's function (NEGF) method.

III. RESULTS AND DISCUSSION

A. Geometric and electronic properties of MoSSe and tellurene

We first investigate the geometric structure and electronic properties of pristine MoSSe and Te monolayers. Based on

the minimization of the total energy, we optimize the lattice parameters from a unit cell of MoSSe and Te monolayers. For the hexagonal MoSSe monolayer, $a = b = 3.25 \text{ \AA}$, and $a = 4.23 \text{ \AA}$ and $b = 5.69 \text{ \AA}$ for the Te unit cell. The results are in good agreement with the previous theoretical results [19–21]. As shown in Fig. 1(a), the Janus MoSSe monolayer is composed of a Mo atomic layer covalently bonded to S and Se atomic layers, which can be regarded as a modified 2H-MoS₂ (MoSe₂) monolayer by surface selenium (sulfur) reaction on one side [5,6]. Because of a strong planar asymmetry due to different atomic species on each side of the metal layer, a large out-of-plane polarization will be induced in Janus MoSSe, where the electrons are generally photoexcited from the negatively charged atoms to the positively charged ones [36]. β -Te with trigonal point group has helical chains parallel to the x axis, where each atom is covalently bonded to the neighboring atom within the chain and the chains pile up in the y direction constituting a zigzag orientation [14], as shown in Fig. 1(b). Based on HSE06 functional, as shown in Figs. 1(c) and 1(d), both monolayer MoSSe and Te belong to direct band gap semiconductors, with the band gap of 2.05 eV for MoSSe, 1.36 eV for Te monolayer, which indicate that the band gap matches up with the maximum of the solar spectrum and show a preferable efficiency of light absorption. For Te monolayer, the spin-orbital coupling effects is also considered, which induces an indirect-to-direct band gap transformation. The valence band minimum (VBM) is well dispersed while the conduction band minimum (CBM) is much more flat, which indicates a light hole and heavy electron carriers transport properties. The effective masses of the both monolayers are calculated by HSE06 functional as shown in Table I.

B. Electronic properties of 2D heterostructures

For the MoSSe/Te and MoSeS/Te heterostructures, the variation of binding energy E_b with the interlayer distance is calculated, as shown in Fig. 2(c). The binding energy for the MoSSe/Te heterobilayer is up to -1.19 and -1.09 eV for MoSeS/Te and the equilibrium distance is calculated to be 3.09 and 2.96 \AA , which has the same order of magnitude as other typical vdW heterostructures [37,38]. For

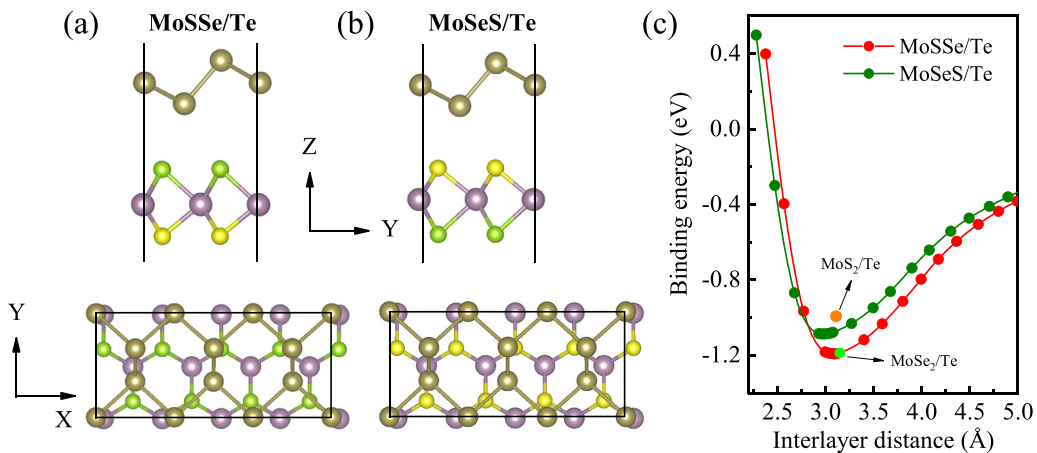


FIG. 2. (a) and (b) Side and top views of MoSSe/Te and MoSeS/Te heterobilayers. (c) The variation of the binding energy as function of interlayer distances in MoSSe/Te and MoSeS/Te heterobilayer.

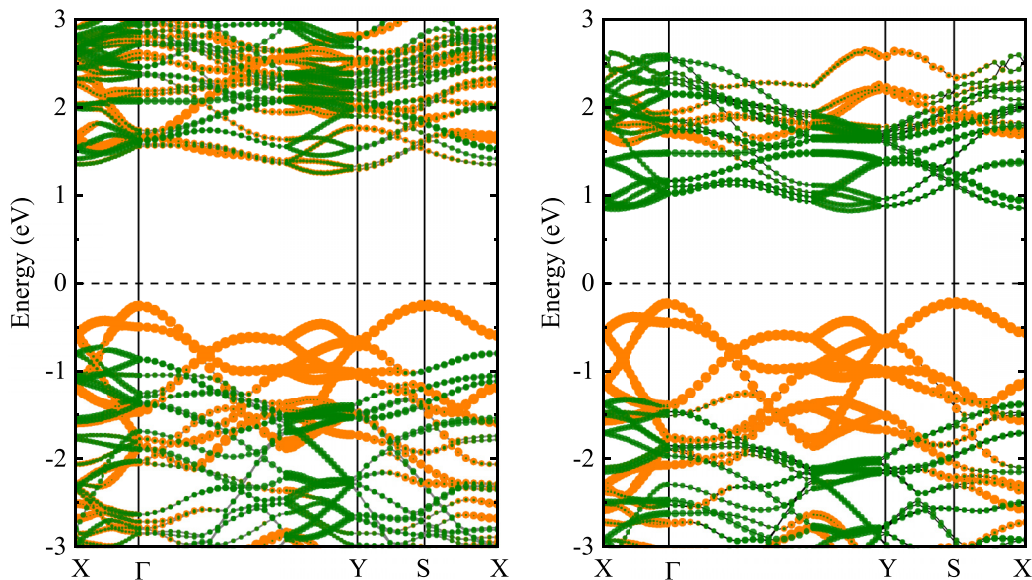


FIG. 3. (a) and (b) Calculated projected band structures of the MoSSe/Te and MoSeS/Te heterostructures based on HSE06. The orange circle represents the electron orbits of Te and the green circle represents the electron orbits of MoSSe, respectively.

comparison, the binding energy of MoS₂/Te and MoSe₂/Te heterostructures are also marked in Fig. 2(c), which show that the binding energy $E_{\text{MoS}_2/\text{Te}} > E_{\text{MoSeS}/\text{Te}} > E_{\text{MoSe}_2/\text{Te}} = E_{\text{MoSSe}/\text{Te}}$. The more negative binding energy can be well explained by an enhancement of interlayer hybridization as a result of charge redistribution in the Janus MoSSe and Te interface. Besides, our theoretical results are also confirmed by the experiment in which Zhang *et al.* found that a broken symmetry strongly enhances the vdW interlayer coupling by as much as 13.2% when forming MoSSe/MoS₂ heterostructure as compared to the pristine MoS₂ counterparts [39]. It indicates that the MoSSe/Te vdW heterostructures are more stable than other vdW heterostructures and it is feasible to be formed through modified 2H-MoSe₂ monolayer by surface sulfur reaction.

Figures 3(a) and 3(b) show the projected band distribution of the MoSSe/Te and MoSeS/Te heterostructures in their respective equilibrium configurations. Both MoSSe/Te and MoSeS/Te exhibit type-II band alignment with an indirect band gap with 1.50 and 1.05 eV under the HSE06 method, respectively, as shown in Table II. It is expected that the type-II band alignment can drive the photogenerated electrons and holes to move in opposite directions, which can result in spatial separation of the electrons and holes on different layers of the heterostructures. Obviously the VBM is contributed by

TABLE II. Calculated equilibrium interlayer distance d_0 (Å), binding energy E_b (meV/per atom), work functions W (eV), band gaps (eV) (PBE/HSE06), and potential differences $\Delta\Phi$ (eV).

	d_0	E_b	W	E_g^{PBE}	E_g^{HSE06}	$\Delta\Phi$
MoSSe			5.63	1.66	2.05	0.76
Tellurene			4.60	1.00	1.36	0
MoSSe/Te	3.18	-121	5.38	1.01	1.50	0.75
MoSeS/Te	3.07	-132	4.65	0.65	1.05	0.60

the Te monolayer, while the CBM comes mainly from MoSSe for two heterostackings. In Figs. 4(a)–4(d) we calculated the total density of states (TDOS) and the corresponding projected density of states (PDOS) with energy between -3 and 3 eV to analyze the electronic structures of the MoSSe/Te and MoSeS/Te vdW heterostructures. As shown in Fig. 4(c), the density of states of Mo-4*d* matches well with that of Te-5*p* at the energy around CBM in MoSSe/Te vdW heterostructure, where a strong *p-d* orbital hybridization interaction led to a considerable number of overlapping states at the CBM for MoSSe/Te heterostructure interface. The photoexcited holes are spatially separated on Te layer, while the overlapping states lead to strong coupling states of CBM, which accelerated the carrier injection from Te layer to Janus MoSSe layer. Thus, nearly perfect band alignment appears between Janus MoSSe and Te sheets in the MoSSe/Te heterostructure. The conduction band offset (CBO) ΔE_c between the two components are gapless for MoSSe/Te, which indicate a high electronic injection efficiency as donor, as shown in Fig. 4(e). By contrast, as shown in Fig. 4(d), we can see that the density of states of Te-5*p* shift up to about 0.6 eV, which do not show the over enhancement of orbital hybridization interaction. Furthermore, the decomposed charge densities of the two heterostructures are shown in Fig. 4(f). When the Te layer is contacted with selenium (Se) surface of Janus MoSSe, the CBM are contributed jointly by MoSSe and Te components, which is consistent with the projected band structure. Therefore, a considerable number of overlapping states are observed within the CBM, which induced an enhancement of interfacial orbital hybridization interaction.

C. Device performance and PCE of the excitonic solar cells

Figure 5(a) shows the schematic model of the device based on MoSSe/Te heterobilayer. It contains a center scattering region, which is sandwiched by two semi-infinite electrodes

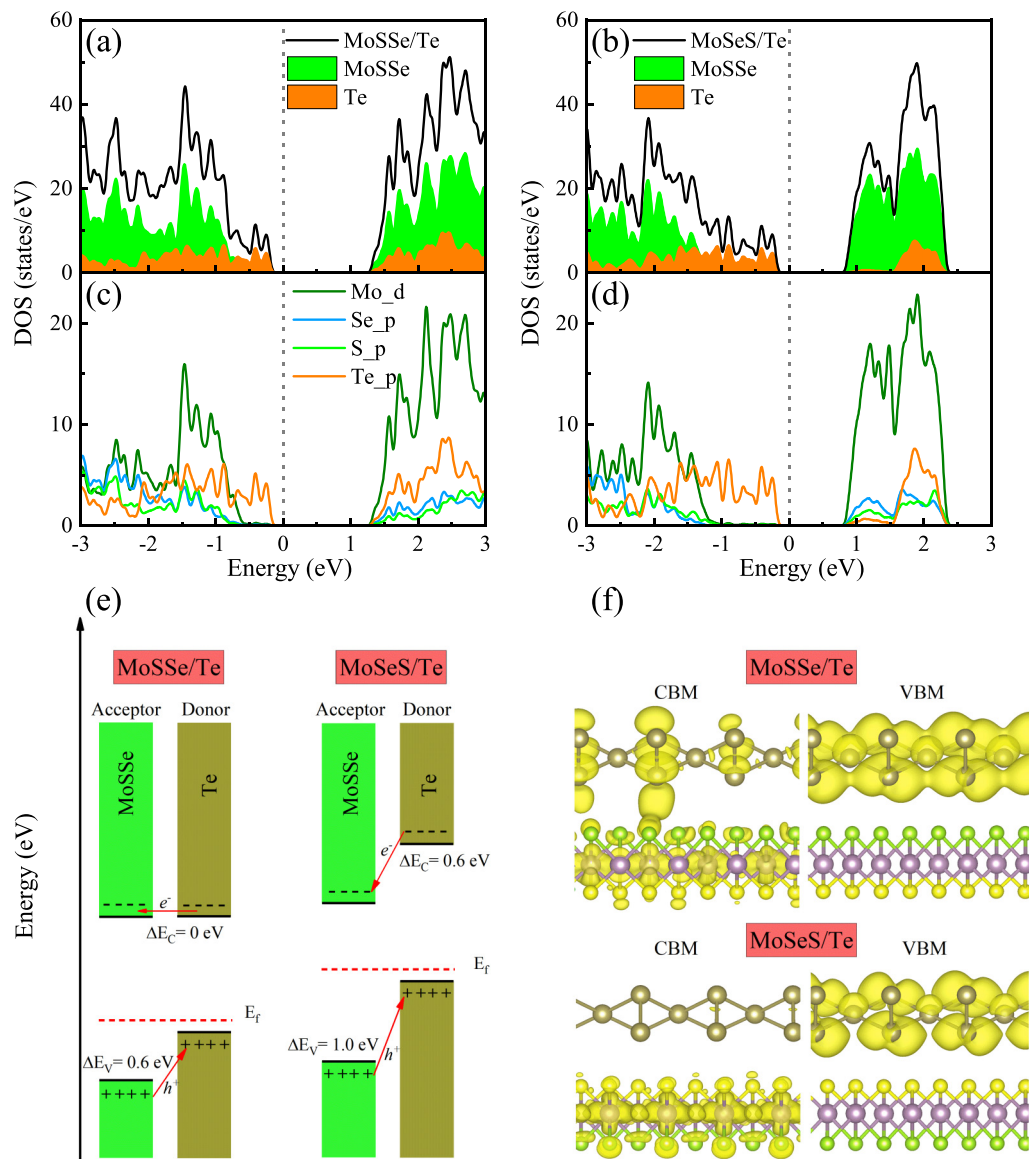


FIG. 4. (a)–(d) Calculated TDOS and the PDOS for the MoSSe/Te and MoSeS/Te heterostructures based on HSE06. The vertical red dotted line represents the Fermi level. (e) Schematic diagram of the type-II donor-acceptor band alignment at HSE06 level. The ΔE_c and ΔE_v represents the conduction band and valence band offsets, respectively. (f) Side views of band decomposed charge densities of MoSSe/Te and MoSeS/Te heterostructures.

(source and drain). To drive the photogenerated carriers flow from the source to drain electrodes, an external bias voltage with the value of 0.2 V is applied between them. It should be noted that the external bias voltage applied here has little influence on the photocurrents, as it is much smaller than the band gap. The photon energy dependence of current density is evaluated under standard test conditions (i.e., AM 1.5 spectral illumination of 1000 W m^{-2}). As shown in Fig. 5(b), the photocurrent density increased rapidly when the photon energy reached about 1.0 eV, which agrees well with the calculated band gap above by the PBE method. This photocurrent originates from interlayer excitations, in which the conduction band and valence band are contributed by different layers of the heterostructure. The maximum photocurrent densities can reach as high as 3.2 A/cm^2 at a photon energy of 1.36 eV, which can be mainly due to the intralayer exci-

tonic contribution [9]. It exceeds those of bilayer MoSSe and 20 nm thin-film silicon devices displaying a bright application prospect. To further characterize the optical performance of MoSSe/Te heterostructure, the calculated optical absorption coefficient $\alpha(\omega)$ as a function of wavelength from the MoSSe/Te heterobilayer and the corresponding monolayers is shown in Fig. 5(c). Compared to MoSSe monolayer, the Te shows much stronger absorption coefficient in the visible light region of 390–760 nm. Moreover, the MoSSe/Te heterobilayer shows wider absorption range and higher optical absorption, which displays an obvious enhancement, as compared with the isolated layers. The absorption coefficients can reach $5 \times 10^5 \text{ cm}^{-1}$ around the wavelength of 400 nm. The enhancement effect of optical absorption performance can be ascribed to the strengthened interlayer hybridization interaction and charge transfer at the interface. The hybridization

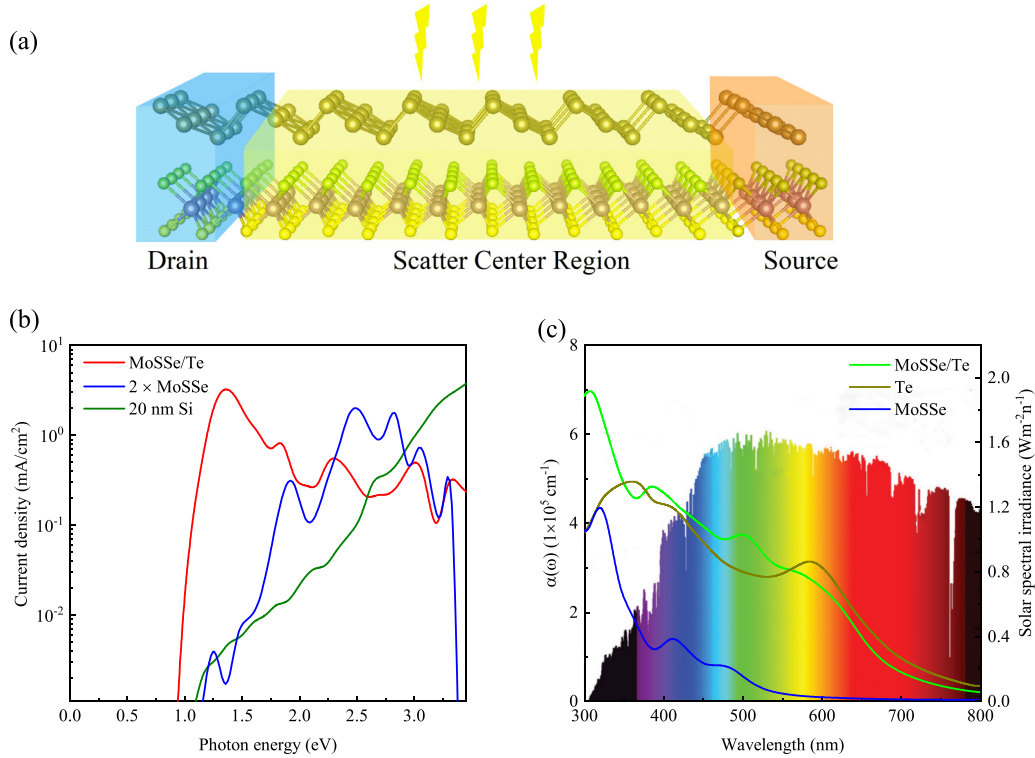


FIG. 5. (a) Schematic diagram of the device based on MoSSe/Te heterostructure with two probes shadowed in blue and orange. The source and drain are electrodes located on the two sides of the center scattering region (yellow region). (b) Photocurrent density as a function of photon energy for the MoSSe/Te heterostructure, bilayer MoSSe, as well as a 20 nm silicon thin film. The current density was calculated under the illumination by the AM 1.5 standard solar spectrum with the photon flux of $1/\text{\AA}^2 \text{ s}$ [34]. (c) The optical absorption coefficient α of isolated Te, MoSSe monolayers, and MoSSe/Te heterobilayer, respectively. The colored area represents the reference solar spectral irradiance at air mass 1.5.

interaction can induce new optical transitions between overlapped electronic states and enhancing optical absorption intensity in heterojunction solar cells. Hence, the MoSSe/Te vdWH are promising solar absorbers for highly efficient solar cells and photovoltaic devices.

Moreover, we estimate the PCE of the heterostructures by the method proposed by Scharber *et al.*, which is widely used in efficiency estimation [40]. The maximum PCE of heterostructure excitonic solar cells can be described as

$$\eta = \frac{J_{\text{SC}} V_{\text{OC}} \beta_{\text{FF}}}{P_{\text{solar}}} = \frac{0.65(E_g^d - \Delta E_c - 0.3) \int_{E_g^d}^{\infty} \frac{P(\hbar\omega)}{\hbar\omega} d(\hbar\omega)}{\int_0^{\infty} P(\hbar\omega) \hbar\omega}, \quad (7)$$

where 0.65 is the empirical value for the band-fill factor, and E_g^d and ΔE_c is the donor band gap and conduction band offset, respectively. The $(E_g^d - \Delta E_c - 0.3)$ represents the maximum open circuit voltage, and the value of 0.3 in the equation is an empirical factor that has been discussed and can be taken from Ref. [40]. $P(\hbar\omega)$ represents the AM 1.5 solar energy flux at the value of $\hbar\omega$ for photon energy. The integral term in the numerator is the short-circuit current density (J_{sc}) assuming external quantum efficiency to be 100%. The energy integral from 0 to infinity in the denominator is the power of incident solar radiation. The direct consequence of Eq. (7) means that reducing the band gap of a heterostructure does not necessarily induce a larger efficiency, since the V_{oc} of the device might be altered. With this equation, Scharber *et al.*

were able to calculate the efficiency of single-junction cells as a function of the donor band gap and its LUMO level, assuming a fill factor of 0.65 and a constant external quantum efficiency of 65%. It is very instructive to confront this model to the two-dimensional excitonic solar cells reported in the literature.

By using the formula (7), we predict the PCE of the two heterostructures, as shown in Fig. 6. The PCE of MoSSe/Te heterojunctions is calculated to be as high as 22.6%, whereas 9.1% for MoSeS/Te. The high PCE of MoSSe/Te is mainly due to the suitable donor band gap of tellurene and its perfect band alignment. The present value is higher than those from GeSe/SnS (18%) [41], phosphorene/MoS₂ (17.5%) [42], GaSe/GeS (16.8% at 2% strain) [37], and comparable or even higher than the newly designed Te/WTe₂ (22.5%) and Te/MoTe₂ (20.1%) heterostructures [22]. The high solar-to-electricity energy conversion efficiency obtained in this work by an orbital hybridization engineering in heterostructure interface can help to design improved excitonic solar cells and broaden the applicability of the Janus MoSSe and Te in the field of photovoltaics device.

D. Photocatalytic water splitting

Production of hydrogen and oxygen via trapping into the endless solar energy through photocatalysis is a promising way to produce clean chemical energy and hopefully

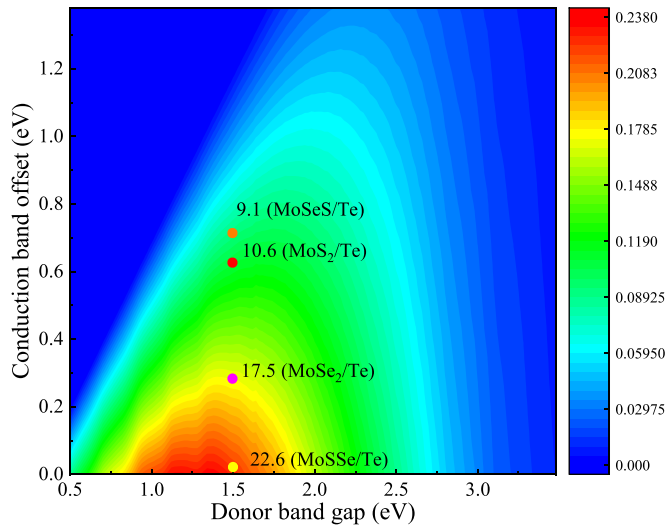


FIG. 6. The PCE diagram of MoSSe/Te, MoSeS/Te heterostructure solar cells. The MoS₂/Te and MoSe₂/Te are provided for reference [22]. The PCE is determined by the band gap of the donor (E_g) and the conduction band offset (ΔE_C) between donor and acceptor.

provide a sustainable solution for environmental problems. Here we explore the photocatalytic properties for the MoSSe/Te and MoSeS/Te vdW heterostructures. Apart from absorption spectrum, the band edge position is another important factor that needs to be considered in photocatalytic water splitting. As the water redox potential depends on the pH value [43,44], where the standard oxidation potential of O₂/H₂O can be calculated by $E_{O_2/H_2O} = -5.67 \text{ eV} + \text{pH} \times 0.059 \text{ eV}$, and the reduction potential for H⁺/H₂ is determined by $E_{H^+/H_2} = -4.44 \text{ eV} + \text{pH} \times 0.059 \text{ eV}$. Thus, the redox potential in acidic environment (pH = 0) and neutral environment (pH = 7) are both studied, as marked by the blue and red dotted lines in Fig. 7. The calculated band-edge positions of Te and Janus MoSSe monolayers show their potentials of water splitting before contact. For Janus MoSSe

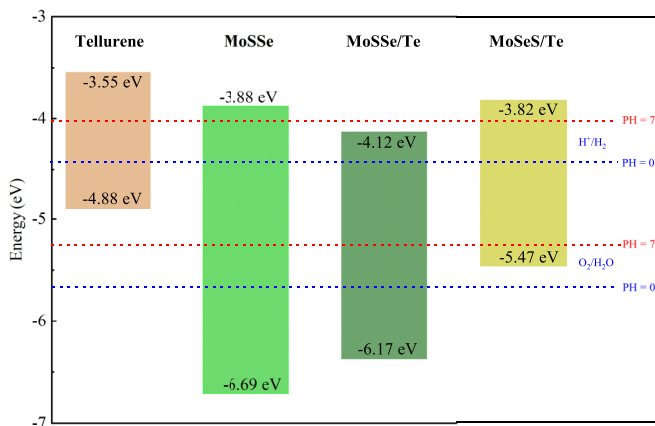


FIG. 7. The valence band (VB) and conduction band (CB) edge alignment of Te, MoSSe, and MoSSe/Te vdW heterostructure and the standard oxidation and reduction potentials for water splitting into O₂/H₂O and H₊/H₂.

monolayer, the calculated band-edge positions span from -3.88 to -6.69 eV, which perfectly satisfy the conditions of photocatalytic water splitting both for pH = 0 and pH = 7, indicating that the MoSSe monolayer is a good candidate for photocatalysis. It should be noted that the band-edge positions are calculated by subtracting the electrostatic potential of the two sides of vacuum level from the CBM and VBM, respectively [45]. The band gap between VBM and CBM is 2.81 eV, which is equal to the sum of intrinsic band gap and the potential difference. The plane-average electrostatic potential difference long the z direction are shown in Figs. 8(a)–8(d), respectively. Due to the out-of-plane asymmetry in Janus MoSSe, a potential difference of 0.76 eV is found between the two sides of vacuum level, as shown in Fig. 8(a). Thus, a built-in intrinsic polarization electric field will be induced along the direction from right to left vacuum level. According to the newly proposed photocatalytic water splitting reaction mechanism [11], the large potentials difference between the left and right vacuum level can bend the band energy level, breaking the conventional limitation of 1.23 eV for band gap of photocatalysts. On the basis of photocatalytic water splitting reactions: $4\text{H}_2\text{O} + 4e^- \xrightarrow{\text{photo}} 2\text{H}_2 + 4\text{OH}^-$, $2\text{H}_2\text{O} + 4h^+ \xrightarrow{\text{photo}} \text{O}_2 + 4\text{H}^+$, in which the polarization driven hydrogen production mainly occurs in the Se surface, while the process of oxygen generation occurs in the left sulfur (S) atoms. Two different reactions occurring in different surface with polarization enhanced carriers separation would benefit for improving the photocatalytic efficiency. As a contrast, as shown in Fig. 8(b), $\Delta\phi$ is zero for Te monolayer, as the Te monolayer is a nonpolarized 2D material. Thus, for Te monolayer, the band-edge positions span from -3.55 to -4.88 eV, not satisfying the conditions of photocatalytic water splitting for pH = 0 nor pH = 7.

When the Janus MoSSe comes into contact with the Te monolayer and forms heterobilayers, depending on different contact interface, an induced polarization field with opposite direction will cross the tellurene. The electrostatic potential difference of the two models of heterostructures are shown in Figs. 8(c) and 8(d). The plane-average electrostatic potential difference of 0.75 and 0.60 eV is found between the two sides of vacuum level. As a whole system, the electrostatic potential differences between MoSSe and Te layer will induce a band bending. Thus, the band-edge positions of MoSSe/Te span from -4.12 to -6.17 eV, which meets the requirements of photocatalytic water splitting at pH = 0, as shown in Fig. 7. The band-edge positions of MoSeS/Te span from -3.82 to -5.47 eV, which meets requirements of photocatalytic water splitting at pH = 7. Therefore, the type-II Janus MoSeS and Te combined vdW heterostructures are suitable for the photogenerated electrons and holes to dissociate water into H₊/H₂ and O₂/H₂O, making them promising for photocatalytic water splitting. Furthermore, the 2D polarized material-based MoSSe/Te and MoSeS/Te vdW heterostructures preserve the advantageous properties, such as the unique dipole-induced internal electric field and surface polarization modulation. Hence, the MoSSe/Te and MoSeS/Te heterostructures are interesting materials for photovoltaic application, which suggests them as promising for low-cost and large-scale production of solar hydrogen.

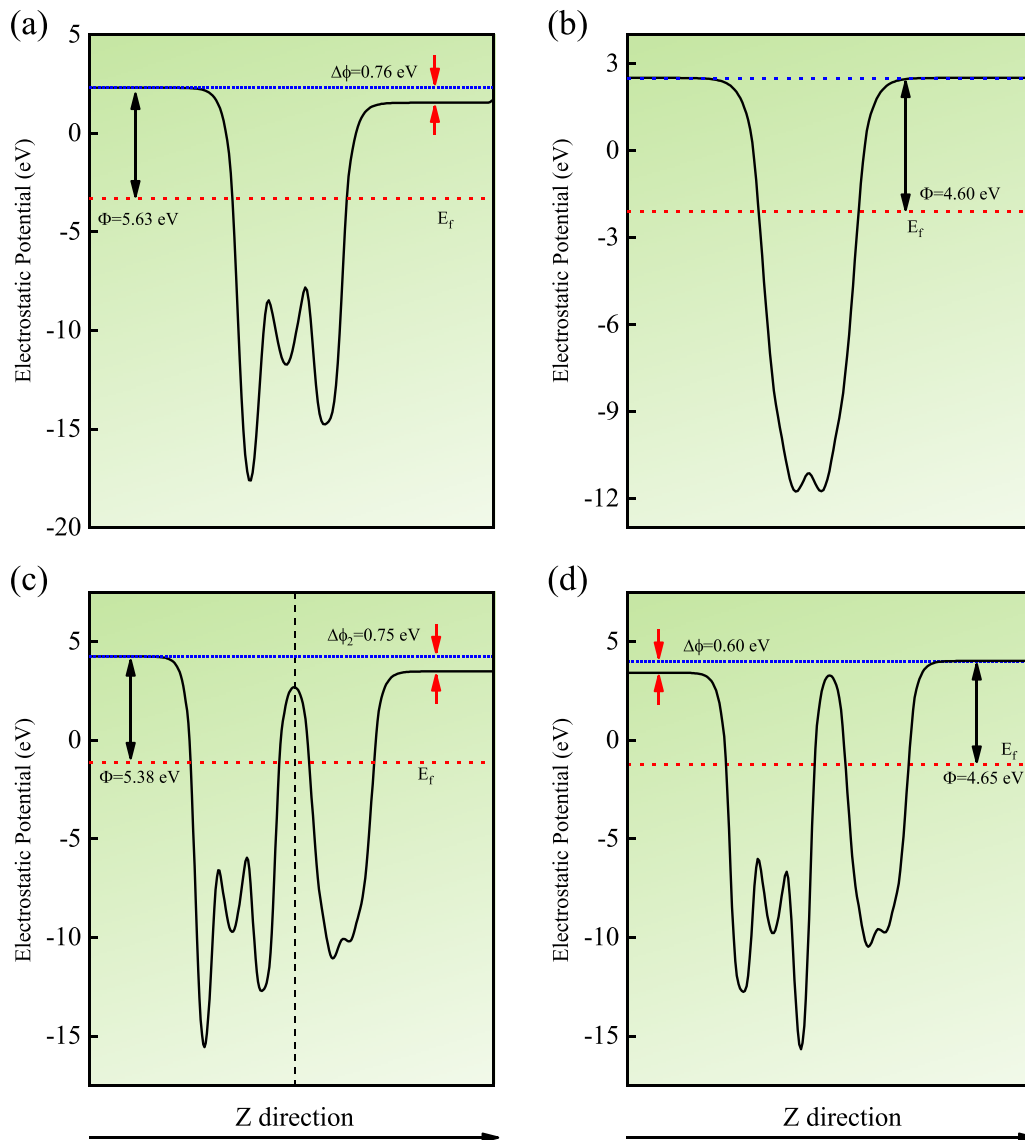


FIG. 8. (a)–(d) Planar average of the electrostatic potential difference versus atomic layers for MoSSe monolayer, Te monolayer, and MoSSe/Te and MoSeS/Te heterobilayers, respectively.

IV. CONCLUSIONS

In summary, we theoretically report an enhancement phenomenon of interlayer orbital hybridization at MoSSe/tellurene vdW interface. The charge density of two components in MoSSe/Te are overlapped at conduction band minimum, which features a highly efficient excitonic solar cells with a PCE of 22.6%. Moreover, the absorbance coefficient is up to $\sim 7 \times 10^5 \text{ cm}^{-1}$ from the UV to visible light region. Combined with the nonequilibrium Green's function method, the calculated maximum photoinduced current density under visible-light radiation, the heterobilayer, is up to 3.2 mA cm^{-2} , which remarkably exceeds that of the thin-film silicon and bilayer MoSSe devices. Furthermore, the superior photocatalytic activities of MoSSe and Te combined heterostructures are solidly revealed and expected. We believe that the present work can offer guidelines for the design of newly MoSSe and Te based vdW heterostructures and the exploration of their potential

applications in photovoltaic, optical devices and photocatalytic fields.

ACKNOWLEDGMENTS

This work was financially supported by the National Natural Science Foundation of China (Grants No. 91833303, No. 61974043, No. 61805081, No. 62074058, and No. 62090013), the National Key Research and Development Program of China (Grants No. 2019YFB2203400, and No. 2017YFA0303403), Projects of Science and Technology Commission of Shanghai Municipality (Grants No. 18JC1412400, No. 18YF1407000, No. 18YF1407200, and No. 19511120100), China Postdoctoral Science Foundation (2020TQ0099 and 2020M681222), and the Program for Professor of Special Appointment (Eastern Scholar) at Shanghai Institutions of Higher Learning and Shanghai Pujiang Program (20PJ1403600).

- [1] L.-J. Zhou, Y.-F. Zhang, and L.-M. Wu, *Nano Lett.* **13**, 5431 (2013).
- [2] H. C. Po, L. Zou, A. Vishwanath, and T. Senthil, *Phys. Rev. X* **8**, 031089 (2018).
- [3] Y. Cao, V. Fatemi, A. Demir, S. Fang, S. L. Tomarken, J. Y. Luo, J. D. Sanchez-Yamagishi, K. Watanabe, T. Taniguchi, E. Kaxiras, R. C. Ashoori, and P. Jarillo-Herrero, *Nature (London)* **556**, 80 (2018).
- [4] G. Hu, Q. Ou, G. Si, Y. Wu, J. Wu, Z. Dai, A. Krasnok, Y. Mazor, Q. Zhang, Q. Bao, C.-W. Qiu, and A. Alù, *Nature (London)* **582**, 209 (2020).
- [5] A.-Y. Lu, H. Zhu, J. Xiao, C.-P. Chuu, Y. Han, M.-H. Chiu, C.-C. Cheng, C.-W. Yang, K.-H. Wei, Y. Yang, Y. Wang, D. Sokaras, D. Nordlund, P. Yang, D. A. Muller, M.-Y. Chou, X. Zhang, and L.-J. Li, *Nat. Nanotechnol.* **12**, 744 (2017).
- [6] J. Zhang, S. Jia, I. Kholmanov, L. Dong, D. Er, W. Chen, H. Guo, Z. Jin, V. B. Shenoy, L. Shi, and J. Lou, *ACS Nano* **11**, 8192 (2017).
- [7] L. Dong, J. Lou, and V. B. Shenoy, *ACS Nano* **11**, 8242 (2017).
- [8] S. Jia, A. Bandyopadhyay, H. Kumar, J. Zhang, W. Wang, T. Zhai, V. B. Shenoy, and J. Lou, *Nanoscale* **12**, 10723 (2020).
- [9] M. Palsgaard, T. Gunst, T. Markussen, K. S. Thygesen, and M. Brandbyge, *Nano Lett.* **18**, 7275 (2018).
- [10] H. Jin, T. Wang, Z.-R. Gong, C. Long, and Y. Dai, *Nanoscale* **10**, 19310 (2018).
- [11] X. X. Li, Z. Y. Li, and J. L. Yang, *Phys. Rev. Lett.* **112**, 018301 (2014).
- [12] Y. Ji, M. Yang, H. Lin, T. Hou, L. Wang, Y. Li, and S.-T. Lee, *J. Phys. Chem. C* **122**, 3123 (2018).
- [13] X. Ma, X. Wu, H. D. Wang, and Y. C. Wang, *J. Mater. Chem. A* **6**, 2295 (2018).
- [14] Z. Zhu, X. Cai, S. Yi, J. Chen, Y. Dai, C. Niu, Z. Guo, M. Xie, F. Liu, J. H. Cho, Y. Jia, and Z. Y. Zhang, *Phys. Rev. Lett.* **119**, 106101 (2017).
- [15] L. Xian, A. P. Paz, E. Bianco, P. M. Ajayan, and A. Rubio, *2D Mater.* **4**, 041003 (2017).
- [16] Y. Wang, G. Qiu, R. Wang, S. Huang, Q. Wang, Y. Liu, Y. Du, W. A. Goddard, M. J. Kim, X. Xu, P. D. Ye, and W. Wu, *Nat. Electron.* **1**, 228236 (2018).
- [17] Y. Du, G. Qiu, Y. Wang, M. Si, X. Xu, W. Wu, and P. D. Ye, *Nano Lett.* **17**, 3965 (2017).
- [18] S. Gao, Y. Wang, R. Wang, and W. Wu, *Semicond. Sci. Technol.* **32**, 104004 (2017).
- [19] J. Qiao, Y. Pan, F. Yang, C. Wang, Y. Chai, and W. Ji, *Sci. Bull.* **63**, 159 (2018).
- [20] X. H. Wang, D. W. Wang, A. J. Yang, N. Koratkar, J. F. Chu, P. L. Lv, and M. Z. Rong, *Phys. Chem. Chem. Phys.* **20**, 4058 (2018).
- [21] Y. Wang, C. Xiao, M. Chen, C. Hua, J. Zou, C. Wu, J. Jiang, S. A. Yang, Y. Lu, and W. Ji, *Mater. Horiz.* **5**, 521 (2018).
- [22] K. Wu, H. Ma, Y. Gao, W. Hu, and J. Yang, *J. Mater. Chem. A* **7**, 7430 (2019).
- [23] P. E. Blöchl, *Phys. Rev. B* **50**, 17953 (1994).
- [24] G. Kresse and J. Hafner, *Phys. Rev. B* **47**, 558 (1993).
- [25] G. Kresse and J. Hafner, *Phys. Rev. B* **49**, 14251 (1994).
- [26] J. P. Perdew, K. Burke, and M. Ernzerhof, *Phys. Rev. Lett.* **77**, 3865 (1996).
- [27] T. Kerber, M. Sierka, and J. Sauer, *J. Comput. Chem.* **29**, 2088 (2008).
- [28] S. Grimme, J. Antony, S. Ehrlich, and H. Krieg, *J. Chem. Phys.* **132**, 154104 (2010).
- [29] J. Neugebauer and M. Scheffler, *Phys. Rev. B* **46**, 16067 (1992).
- [30] M. Marsman, J. Paier, A. Stroppa, and G. Kresse, *J. Phys.: Condens. Matter* **20**, 064201 (2008).
- [31] S. Smidstrup, T. Markussen, P. Vancraeyveld, J. Wellendorff, J. Schneider, T. Gunst, B. Verstichel, D. Stradi, P. A. Khomyakov, U. G. Vej-Hansen, M.-E. Lee, S. T. Chill, F. Rasmussen, G. Penazzi, F. Corsetti, A. Ojanpera, K. Jensen, M. L. N. Palsgaard, U. Martinez, A. Blom *et al.* *J. Phys.: Condens. Matter* **32**, 15901 (2019).
- [32] J. Chen, Y. Hu, and H. Guo, *Phys. Rev. B* **85**, 155441 (2012).
- [33] C. Rivas, R. Lake, G. Klimeck, W. R. Frensley, M. V. Fischetti, P. E. Thompson, and S. L. Rommel, and P. R. Berger, *Appl. Phys. Lett.* **78**, 814 (2001).
- [34] M. Palsgaard, T. Markussen, T. Gunst, M. Brandbyge, and K. Stokbro, *Phys. Rev. Appl.* **10**, 014026 (2018).
- [35] B. J. Huang, P. E. Yang, Y. P. Lin, B. Y. Lin, H. J. Chen, R. C. Lai, and J. S. Cheng, *Sol. Energy* **85**, 388 (2018).
- [36] B. Zhou, K. Jiang, L. Y. Shang, J. Z. Zhang, Y. W. Li, L. Q. Zhu, S. J. Gong, Z. G. Hu, and J. H. Chu, *J. Mater. Chem. C* **8**, 11160 (2020).
- [37] B. Zhou, S. J. Gong, K. Jiang, L. P. Xu, L. Y. Shang, J. Z. Zhang, Z. G. Hu, and J. H. Chu, *J. Mater. Chem. C* **8**, 89 (2020).
- [38] B. Zhou, S. J. Gong, K. Jiang, L. P. Xu, L. Q. Zhu, L. Y. Shang, Y. W. Li, Z. G. Hu, and J. H. Chu, *J. Phys.: Condens. Matter* **32**, 055703 (2020).
- [39] K. Zhang, Y. Guo, Q. Ji, A.-Y. Lu, C. Su, H. Wang, A. A. Puzos, D. B. Geohegan, X. Qian, S. Fang, E. Kaxiras, J. Kong, and S. Huang, *J. Am. Chem. Soc.* **142**, 17499 (2020).
- [40] M. C. Scharber, D. Mühlbacher, M. Koppe, P. Denk, C. Waldauf, A. J. Heeger, and C. J. Brabec, *Adv. Mater.* **18**, 789 (2006).
- [41] X. Lv, W. Wei, C. Mu, B. Huang, and Y. Dai, *J. Mater. Chem. A* **6**, 5032 (2018).
- [42] S. Kaur, A. Kumar, S. Srivastava, K. Tankeshwar, and R. Pandey, *J. Phys. Chem. C* **122**, 26032 (2018).
- [43] H. L. L. Zhuang and R. G. Hennig, *Chem. Mater.* **25**, 3232 (2013).
- [44] H. C. Yang, J. J. Li, L. Yu, B. B. Huang, Y. Ma, and Y. Dai, *J. Mater. Chem. A* **6**, 4161 (2018).
- [45] S. R. Wei, J. W. Li, X. Q. Liao, H. Jin, and Y. D. Wei, *J. Phys. Chem. C* **123**, 22570 (2019).